# Recent mechanical weakening of the Arctic sea ice cover as revealed from larger inertial oscillations

Florent Gimbert, Nicolas C. Jourdain, David Marsan, Jérôme Weiss, Bernard Barnier

# Recent mechanical weakening of the Arctic sea ice cover as revealed from larger inertial oscillations

F. Gimbert,[1,2] N. C. Jourdain,[3] D. Marsan,[4] J. Weiss,[2] and B. Barnier[3]

Received 27 September 2011; revised 10 February 2012; accepted 4 April 2012; published 19 May 2012.

[1] We present a simple and analytical ocean boundary layer-sea ice coupled dynamical model that we apply to the modeling of Arctic sea ice motion in the frequency domain, and particularly in the inertial range. This study further complements our related work in an unpublished paper where the sea ice cover response to the Coriolis forcing has been studied. This analytical model allows interpretation of the spatial, seasonal and pluriannual dependence of the magnitude of the inertial oscillations detailed in terms of mechanical behavior of the ice cover. In this model, the sea ice mechanical response is simplified through the introduction of a linear internal friction term $K$. A dependence of $K$ allows us to explain the associated dependence of the seasonal and regional Arctic sea ice inertial motion. In addition, a significant decrease of $K$, i.e., a mechanical weakening of the sea ice cover, is observed for the period 2002–2008 compared to 1979–2001, for the entire Arctic in both seasons. These results show that the regional, seasonal and pluriannual variations of sea ice inertial motion are not only the trivial consequence of simultaneous variations of thickness and concentration (and so of ice mass per unit area). Instead, the shrinking and thinning of the Arctic sea ice cover over the last few decades has induced a mechanical weakening, which in turns has favored sea ice fracturing and deformation.

**Citation:** Gimbert, F., N. C. Jourdain, D. Marsan, J. Weiss, and B. Barnier (2012), Recent mechanical weakening of the Arctic sea ice cover as revealed from larger inertial oscillations, *J. Geophys. Res.*, *117*, C00J12, doi:10.1029/2011JC007633.

## 1. Introduction

[2] In recent decades, Arctic sea ice underwent a spectacular decline in terms of concentration, extent [*Comiso et al.*, 2008; *Stroeve et al.*, 2008], and average thickness [*Rothrock et al.*, 2008; *Kwok and Rothrock*, 2009]. From this evolution of the sea ice state, that is, of the degree of consolidation of the ice cover, a simultaneous evolution of the magnitude of internal stresses and of the mechanical behavior is expected. In turns, such expected evolution of the sea ice mechanical response should enhance sea ice fracturing, deformation, and drift, as actually observed [*Rampal et al.*, 2009]. To measure such possible mechanical weakening is however difficult. Internal ice stress measurements [*Richter-Menge and Elder*, 1998; *Richter-Menge et al.*, 2002], of great interest to analyze mechanical processes and sea ice rheology at the local scale [*Weiss et al.*, 2007], are limited to local spatial and short timescales. Our approach, performed at the basin and multidecadal scales from the International Arctic Buoy Programme (IABP) data set, consists in the analysis of the response of sea ice to the well-defined Coriolis force. As this specific forcing is constant over time, an evolution of the response, i.e., of ice motion around the inertial frequency $f_0 \approx 2$ cycles.d$^{-1}$ within the arctic basin, would be a signature of a change in the mechanical behavior of the ice cover.

[3] In an unpublished paper (F. Gimbert et al., Sea ice inertial oscillation magnitudes in the Arctic basin, submitted to *The Cryosphere*, 2012), we performed from the same data set a statistical analysis of the magnitude of inertial motion, relatively to the norm of the velocities, and revealed spatial and seasonal patterns in agreement with the corresponding ice concentration and thickness patterns, i.e., inertial motion is more pronounced in regions (Beaufort Sea, eastern Arctic) and seasons (summers) where ice is thinner and less concentrated. This analysis also revealed a significant strengthening of ice inertial motion at the basin scale, in both summer and winter, in recent years. This evolution, we suggested, is likely to be the signature of a mechanical weakening of the ice cover and a decrease of the magnitude of internal stresses. This analysis, however, did not allow to differentiate precisely the direct effect of ice thinning, the effect of a possible modification of vertical penetration of turbulent momentum within the ocean boundary layer, or that of an actual mechanical weakening, onto this strengthening of inertial motion.

[1]Institut des Sciences de la Terre, CNRS, Université Joseph Fourier, Grenoble, France.
[2]Laboratoire de Glaciologie et de Géophysique de l'Environnement, UMR 5183, CNRS, Université Joseph Fourier, Grenoble, France.
[3]Laboratoire des Ecoulements Géophysiques et Industriels, UMR 5519, CNRS, Université Joseph Fourier, Grenoble, France.
[4]Institut des Sciences de la Terre, UMR 7193, CNRS, Université de Savoie, Le Bourget du Lac, France.

Corresponding author: F. Gimbert, Institut des Sciences de la Terre, CNRS, Université Joseph Fourier, BP 53, F-38041 Grenoble CEDEX 9, France. (florent.gimbert@ujf-grenoble.fr)


0148-0227/12/2011JC007633

[4] In the present paper, we present a simple ice-ocean boundary layer coupled dynamical model. As shown below, although crude, this model describes well sea ice motion in the inertial range, its seasonal as well as regional variations, and allows to account for the role of the different factors listed above. A genuine mechanical weakening of the Arctic sea ice cover in recent years is revealed by the model, as changes within the sea ice rheological term are required to explain the observations.

[5] In another hand, this simple ice-ocean boundary layer coupled dynamical model allows to investigate the link between the sea ice properties and the propagation of inertial oscillations within the ocean. Indeed, the Arctic ocean is characterized by a shallow mixed layer depth at near freezing point temperatures. The mixed layer depth is generally small and controlled by the pronounced underlying cold halocline that limits the depth of winter convection. The mixed layer freshwater results from ice melting, rivers runoff, and from the transport of low-salinity Pacific waters. The vertical mixing rate is of high importance, because mixing of warmer deeper layers can heat the mixed layer and affect surface fluxes and the sea ice variability. The observed mixing rate has been found to be small as compared to lower latitudes [*Gregg*, 1989; *Rainville and Winsor*, 2008; *Fer*, 2009]. Relatively high vertical mixing rate are nonetheless found over bottom topographic features, which highlights the role of internal waves in the Arctic basin [*D'Asaro and Morison*, 1992]. These internal waves can be generated by tides [*D'Asaro and Morison*, 1992] or by sea ice motions that generate near inertial currents [*McPhee and Kantha*, 1989; *Pinkel*, 2005; *Lenn et al.*, 2011]. Thus, understanding the variability of the energy transfer from the atmosphere to the ocean, through sea ice, in the inertial range is a major concern. Typical values of the thickness of the mixed layer and the turbulent kinetic energy produced within the ocean mixed layer can be inferred from the model.

## 2. A Simple Ocean-Sea Ice Coupled Dynamical Model

[6] For about 40 years, many works have focused on the modeling of oceanic inertial currents induced by moving storms and fronts because they significantly contribute to the vertical mixing of the global ocean [*Pollard and Millard*, 1970; *Watanabe and Hibiya*, 2002; *Alford*, 2003; *Elipot and Gille*, 2009]. A full description of the propagation of inertial waves requires taking topography, eddies, and the entire momentum equation into account [*D'Asaro et al.*, 1995; *Young and Ben Jelloul*, 1997; *Garrett*, 2001]. However, a focus on the few first inertial periods after the storm passage (i.e., before the propagation of inertial waves toward the thermocline) allows a simplified description of the energy transfer from winds to inertial currents. Thus, a slab model of the oceanic surface boundary layer is suitable for the description of inertial oscillations [*Pollard and Millard*, 1970; *Plueddemann and Farrar*, 2006]. The horizontal pressure gradients may be dropped from the momentum equation if the storm translation speed is greater than the internal wave group velocity (1–3 $m.s^{-1}$), which is the case for most of the storms [*Greatbatch*, 1984].Finally, the nonlinear advection terms may also be dropped from the momentum equation because of their little effect in the ocean response to a moving storm [*Greatbatch*, 1983].

[7] The damping of inertial motions is related to a downward radiation of near-inertial waves excited by inertial pumping, and to the vertical penetration of turbulent momentum related to the shear induced by near-inertial motions [*Park et al.*, 2009, and references therein]. As we need an analytical solution of the ocean mixed layer response, we choose a very idealized description of the damping term: the deep ocean is assumed to be at rest, and the damping term is written as a friction at the base of the ocean surface boundary layer that is proportional to the surface ocean velocity (as, e.g., in *Pollard and Millard* [1970], *Gent et al.* [1983] and *Plueddemann and Farrar* [2006]). The friction velocity that takes place within the ocean surface layer is referred to as $\gamma$ (unit $m.s^{-1}$), so that the induced stress corresponds to $\rho_w \gamma U_w$ (unit $N.m^{-2}$), where $U_w$ and $\rho_w$ are the norm of the ocean surface velocity and the density of the ocean surface layer, respectively. The simplifications mentioned above are assumed to be suitable for the sea ice response to a moving storm, and the resulting sea ice slab model is coupled to the ocean slab model as outlined on Figure 1. The resulting set of coupled momentum equations is

$$\begin{cases} \dfrac{du_i}{dt} = \omega_0 v_i - \dfrac{C_{iw}}{h_i}(u_i - u_w) - K u_i + \dfrac{\tau_x}{\rho_i h_i} \\ \dfrac{dv_i}{dt} = -\omega_0 u_i - \dfrac{C_{iw}}{h_i}(v_i - v_w) - K v_i + \dfrac{\tau_y}{\rho_i h_i} \\ \dfrac{du_w}{dt} = \omega_0 v_w - \dfrac{\gamma}{h_w} u_w - \dfrac{\alpha C_{iw}}{h_w} u_w - u_i + \dfrac{(1-\alpha)}{\rho_w h_w}\tau_x \\ \dfrac{dv_w}{dt} = -\omega_0 u_w - \dfrac{\gamma}{h_w} v_w - \dfrac{\alpha C_{iw}}{h_w}(v_w - v_i) + \dfrac{(1-\alpha)}{\rho_w h_w}\tau_y, \end{cases} \quad (1)$$

where $(u, v)$ are the horizontal velocity components of sea ice (index $i$) and the ocean surface layer (index $w$), $h_i$ and $h_w$ are the thickness of sea ice and the ocean surface layer respectively. The densities of each layer are referred to as $\rho_i$ and $\rho_w$, $\alpha$ is the sea ice surface fraction, and $\omega_0 = 2\pi f_0$ is the Coriolis frequency. The stress at the interface between sea ice and the underlying water is taken as $\rho_w C_{iw}(U_i - U_w)$ (in $N.m^{-2}$), where $U_i$ and $U_w$ are the speed norm of sea ice and ocean surface layer, and $C_{iw}$ is the ice-ocean drag coefficient. Here, we consider that $C_{iw}$ is independent of the velocities $U_i$ and $U_w$. Such a linear form is more suitable for the ocean-ice friction than for the air-ice friction because the air kinematic viscosity is about 10 times smaller than the sea water viscosity, and because currents are slower than winds. The quadratic form would nonetheless be a better approximation because the Reynolds number remains greater than unity, and because the form drag associated with sea ice protuberances is usually defined using a quadratic form [*McPhee and Kantha*, 1989]. However, we use a linear form (as *Heil and Hibler* [2002] and *Weatherly et al.* [1998]) since it allows an analytical solution of (1). For the sake of simplicity, the wind stress $(\tau_x, \tau_y)$ is chosen to be the same on sea ice as on open water (according to *Lepparanta* [2004] the factor between both is typically 1.2).

[8] In this crude model, the internal sea ice friction is taken as a stress equal to $\rho_i K h_i U_i$ (unit $N.m^{-2}$), where $K$

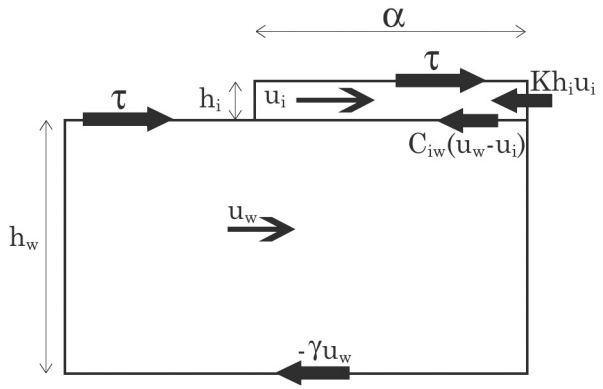


**Figure 1.** Sketch of the sea ice slab model coupled to the ocean slab model following hypotheses discussed in section 2: a sea ice slab (indices i) of thickness $h_i$ is coupled to an ocean layer (indices w) of with $h_w$. Wind stress forcing $\tau$ is applied to both the ice and the water column, with relative weights $\alpha$ and $1 - \alpha$, respectively, where $\alpha$ represents the ice concentration. Friction is present within the ice ($Kh_iu_i$) at the ice-water interface ($C_{iw}(u_w - u_i)$) and at the bottom of the ocean layer ($\gamma u_w$).

(unit $s^{-1}$) is a friction coefficient that represents the inverse of a temporal scale of dissipation. The introduction of such a linear friction term might appear as a strong simplification with regard to the elasto-brittle, i.e., strongly nonlinear, character of sea ice rheology [*Girard et al.*, 2011; *Weiss et al.*, 2007]. However, as shown below, a simple model such as this describes reasonably well the ice behavior in the frequency domain when properly averaged over large spatial and timescales, especially during summer. Instead of performing a mechanical modeling at the fine scale, we here use this model for a comparative study of the sea ice average mechanical behavior between winter and summer, in different regions of the Arctic, or between different periods. This model takes into account the effect of ice thickness (e.g., ice thinning in recent years) and concentration in the momentum balance.

## 3. Solution of the Model Equations

[9] It is convenient to use the complex velocities and stress

$$\begin{cases} \tilde{U}_i = u_i + iv_i \\ \tilde{U}_w = u_w + iv_w \\ \tilde{\tau} = \tau_x + i\tau_y. \end{cases} \tag{2}$$

Hence, equations (1) become

$$\begin{cases} \dfrac{d\tilde{U}_i}{dt} = -i\omega_0\tilde{U}_i - \dfrac{C_{iw}}{h_i}\tilde{U}_i + \dfrac{C_{iw}}{h_i}\tilde{U}_w - K\tilde{U}_i + \dfrac{\tilde{\tau}}{\rho_i h_i} \\ \dfrac{d\tilde{U}_w}{dt} = -i\omega_0\tilde{U}_w - \dfrac{\alpha C_{iw}}{h_w}\tilde{U}_w + \dfrac{\alpha C_{iw}}{h_w}\tilde{U}_i - \dfrac{\gamma}{h_w}\tilde{U}_w + \dfrac{(1-\alpha)}{\rho_w h_w}\tilde{\tau}. \end{cases} \tag{3}$$

[10] Deriving the first equation of (3) with respect to time, and combining to the second equation yields

$$\begin{cases} \dfrac{d^2\tilde{U}_i}{dt^2} + \left(2i\omega_0 + \dfrac{\alpha C_{iw}}{h_w} + \dfrac{C_{iw}}{h_i} + \dfrac{\gamma}{h_w} + K\right)\dfrac{d\tilde{U}_i}{dt} \\ \quad + \left[\left(i\omega_0 + \dfrac{\gamma}{h_w} + \dfrac{\alpha C_{iw}}{h_w}\right)\left(i\omega_0 + \dfrac{C_{iw}}{h_i} + K\right) - \dfrac{\alpha C_{iw}^2}{h_i h_w}\right]\tilde{U}_i \\ \quad = \dfrac{1}{\rho_i h_i}\dfrac{d\tilde{\tau}}{dt} + \left[(1-\alpha)\dfrac{C_{iw}}{\rho_w h_w h_i} + \dfrac{1}{\rho_i h_i}\left(i\omega_0 + \dfrac{\gamma}{h_w} + \dfrac{\alpha C_{iw}}{h_w}\right)\right]\tilde{\tau}, \end{cases} \tag{4}$$

which can be solved in the Fourier's domain to write the transfer function

$$\begin{cases} \hat{G}(\omega) = \dfrac{\hat{U}_i(\omega)}{\hat{\tau}(\omega)} \\ = \dfrac{1}{\rho}\dfrac{\dfrac{1}{h_i h_w}(C_{iw} + \gamma) + i(\omega + \omega_0)\dfrac{1}{h_i}}{\left[\left(-(\omega+\omega_0)^2 + \dfrac{1}{h_w}(\alpha C_{iw} + \gamma)\left(K + \dfrac{C_{iw}}{h_i}\right) - \dfrac{\alpha C_{iw}^2}{h_i h_w}\right) + i(\omega+\omega_0)\left(\dfrac{C_{iw}}{h_i} + \dfrac{\alpha C_{iw}}{h_w} + \dfrac{\gamma}{h_w} + K\right)\right]}, \end{cases} \tag{5}$$

where $\omega = 2\pi f$ and $\rho_i = \rho_w = \rho$ is assumed. Equation (5) shows a resonance when $\omega + \omega_0 = 0$, hence at the negative frequency of $-f_0 \approx -2$ cycles.$d^{-1}$.

[11] This transfer function allows linking between ice velocities and wind stresses, i.e., to express the frequency response of sea ice to a given external forcing as a function of oceanic and sea ice internal parameters. In this analysis, no oceanic data (e.g., velocity) are needed. This is the strength of our method since such data do not exist or are very rare. Aside from the present study, equation (5) could be used to infer angles between the average wind stress and ice motion by looking to its imaginary part at $\omega = 0$ cycle.$d^{-1}$. We here briefly checked that angles predicted by our model were consistent with common observations: by setting values of parameters inferred from section 5.2 and summed up in Table 1, we find average angles varying from $-29°$ to $-37°$, the minus sign indicating an angle in the clockwise direction, i.e., an ice drift deviated toward the right with respect to the wind direction, which is consistent in the northern hemisphere.

## 4. Computation of the Transfer Functions From the Data

[12] We consider eight different ice-tethered buoy data sets, built from the International Arctic Buoy Program

**Table 1.** Model Parameters Used to Compute the Simulations Plotted on Figure 5[a]

| | | | | Fixed Parameters | | Tuning Parameters | | | |
|---|---|---|---|---|---|---|---|---|---|
| | Zone | Season | Data Set | $h_i$ (m) | $\alpha$ | $K$ (days$^{-1}$) | $h_w$ (m) | $\mathcal{T}$ (days) | $M$ |
| Period 1 | Pack zone | Winter | 1 | 4 | 0.98 | 12 | 45 | 52 | 0.151 |
| | Pack zone | Summer | 2 | 3 | 0.9 | 7 | 35 | 40 | 0.172 |
| | Peripheral zone | Winter | 3 | 3 | 0.96 | 11.5 | 45 | 52 | 0.156 |
| | Peripheral zone | Summer | 4 | 2 | 0.82 | 7 | 25 | 29 | 0.244 |
| Period 2 | Pack zone | Winter | 5 | 3.5 | 0.96 | 7.5 | 30 | 35 | 0.182 |
| | Pack zone | Summer | 6 | 2.5 | 0.84 | 5.5 | 25 | 29 | 0.220 |
| | Peripheral zone | Winter | 7 | 2.5 | 0.95 | 8.5 | 20 | 23 | 0.202 |
| | Peripheral zone | Summer | 8 | 1.5 | 0.62 | 4.5 | 10 | 12 | 0.371 |

[a]Here we set $C_{iw} = 5.10^{-4}$ m.s$^{-1}$ and $\gamma = 10^{-5}$ m.s$^{-1}$. The values of $C_{iw}$, $\gamma$ and $h_i$ are typical values taken from the literature. The concentration $\alpha$ is computed from the NSIDC sea ice concentration data set. The modeled transfer functions are adjusted compared to the data by tuning $K$ and $h_w$, since these two parameters play an independent role: $K$ controls the amplitude of the inertial peak while $h_w$ only controls its width.

(IABP) buoys data set (described in more details in an unpublished paper (Gimbert et al., submitted manuscript, 2012)) in the following way. First, two data sets related to 10 day buoy trajectories are constructed: the "central pack" and the "peripheral zone" data set contains buoy positions recorded within the regions delimited on Figure 2 by the blue and red lines, respectively. The central pack consists of thick, highly cohesive perennial sea ice, i.e., is characterized by small inertial oscillations and small $M$ values, where $M$ is defined (Gimbert et al., submitted paper, 2012): $M$ is a non dimensional parameter that evaluate the magnitude of the sea ice velocity at the inertial frequency with respect to the norm of the velocity. This way, the parameter $M$ quantitatively accounts for the sea ice time-dependant inertial oscillation magnitude. In contrast, the peripheral zone is nowadays essentially covered by seasonal sea ice, hence a poorly cohesive cover during the summer months, and so is associated with strong oscillations and large $M$ values. Secondly, each of these two data sets are split following the winter and summer seasons, defined (Gimbert et al., submitted manuscript, 2012) from the annual cycle described by the monthly $M$ values (the summer period goes from July to September and the winter period is the rest of the year). Finally, from these four data sets, we define eight data sets by separating the two periods defined from the pluriannual analysis of $M$ (Gimbert et al., submitted manuscript, 2012): period 1 extending from 1979 to 2001, and period 2 from 2002 to 2008. Each data set are numbered from 1 to 8 as recapitulated in Table 1.

### 4.1. Sea Ice Data

[13] For each 10 day buoy trajectory in any one of the eight data sets, the Fourier transform $\hat{U}_b$ of the buoy velocities is computed following equation 4 of (Gimbert et al., submitted manuscript, 2012). This equation leads to a signed fourier transform of the buoys velocities, in which the inertial frequency is negative and corresponds to $f = -f_0$, since inertial oscillations are associated to a rotation in the clockwise direction in the northern hemisphere. These Fourier transforms thus obtained are then averaged over all trajectories of a given data set. The results, shown in Figure 3a, confirm the following: (1) the existence of seasonal and spatial variations of the inertial oscillation amplitude and (2) the increase of the inertial oscillation amplitude in recent years, more or less marked depending on the data set (e.g., the maximum increase is observed in summer and within the peripheral zone, where the inertial oscillation amplitude varies from 1.16 km.d$^{-1}$ in period 1 to 2.12 km.d$^{-1}$ in period 2, i.e., a 86% increase, and the minimum increase is observed in summer and in the central pack, where the inertial oscillation amplitude varies from 0.59 km.d$^{-1}$ in period 1 to 0.87 km.d$^{-1}$ in period 2, i.e., a 40% increase).

### 4.2. Wind Data (Forcing)

[14] Estimates of the surface winds for each buoy position are obtained from the ERA-Interim data set provided by the ECMWF (http://data-portal.ecmwf.int/data/d/interim_daily/). This data set is a model simulation at a T255 horizontal resolution, including 12 h 4D-VAR assimilation of observations. The 12 h time window for data assimilation introduces an artificial peak in the wind velocity spectrum indifferently present at $f = -2$ and $f = 2$ cycles.d$^{-1}$; in the following, this peak is deleted using a linear interpolation in log-log space between the frequencies $-2.5$ and $-1.5$ cycles.d$^{-1}$ and 1.5 and 2.5 cycles.d$^{-1}$. The outputs used here are 3-hourly, on a regular grid of 0.625° by 0.625°.

[15] For each buoy position $(x_i, y_i)$, we associate the wind velocity components $u_a$ and $v_a$ by looking for the closest value that figures within the ERA-Interim data set. Then for each buoy trajectory of the eight data sets, the Fourier transform $\hat{\tau}_b$ of the wind stress at the buoys locations is computed using a quadratic dependence to the wind speed

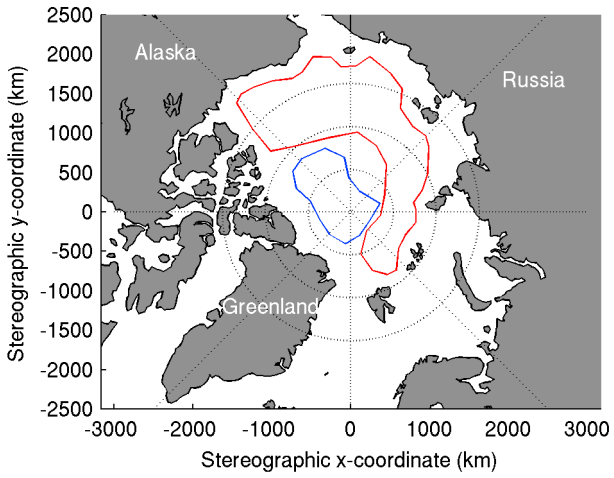


**Figure 2.** Spatial sampling of the 10 days buoy trajectories: peripheral zone (red) and central pack (blue).

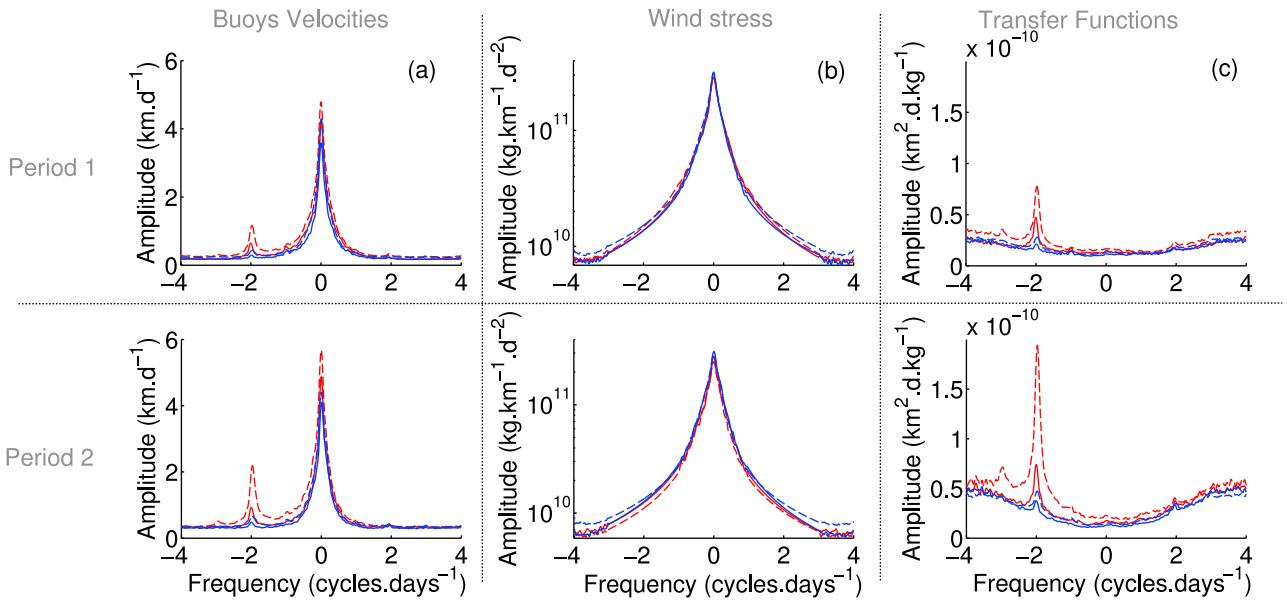


**Figure 3.** Fourier transform of the (a) buoy velocities, (b) wind stress and (c) associated transfer functions for (top) period 1979–2001 and (bottom) period 2002–2008. The red and blue curves correspond respectively to summer and winter. The thick and dashed lines correspond to the pack zone and peripheral zone, respectively.

with a constant drag coefficient $C_a = 0.0012$ [*Hibler*, 1979]. Finally, the Fourier transforms are averaged over all the trajectories, for each data set.

[16] Remarkably, no significant change in the spectrum of the wind forcing with neither the region, the season, nor the period, is obtained from the ERA-Interim data set (Figure 3b).

[17] This is in strong contrast with what is observed for ice velocities in section 4.1, which shows much changes with respect to the season and the period. This underlines the purpose of this study, showing that changes within sea ice (whether they are about changes in sea ice concentration, sea ice thickness or sea ice internal mechanical properties) are necessary to explain these discrepancies. The purpose of this paper is to evaluate the relative contribution of these sea ice properties in the observed overall change, by evaluating changes of sea ice motion relatively to wind forcing from the use of transfer functions.

### 4.3. Transfer Functions

[18] The transfer function amplitudes $|\hat{G}_b|$ computed using $\hat{U}_b$ and $\hat{\tau}_b$ (Figures 3a and 3b) are plotted on Figure 3c. They are roughly symmetric with respect to $f = 0$, except at $f = -f_0$ for which we recognize the inertial oscillation peak with varying amplitude. A plateau characterizes low frequencies, whereas $|\hat{G}_b|$ slightly increases above $f_0$. As there is a significant uncertainty on the buoys' locations (100 to 300 m, depending on the positioning system), we first analyze the effect of such an uncertainty on the transfer function : from a given data set, we add noise on the raw buoys positions $(x_b, y_b)$ by defining $(\widetilde{x_b}, \widetilde{y_b})$ as $\widetilde{x_b} = x_b + \delta x$ and $\widetilde{y_b} = y_b + \delta y$, where $\delta x$ and $\delta y$ are (small) increments randomly picked from a centered gaussian distribution with 300 m standard deviation. Then, a synthetic transfer function is computed from the noisy buoy positions $(\widetilde{x_b}, \widetilde{y_b})$, see Figure 4: the color curves are the transfer function computed from the raw data (here data set number 8 and data set number 1) while the black dashed curve are the respective transfer function computed from the noisy buoy positions. For both of these plots, a good agreement between the two transfer functions is obtained at low frequencies while, at larger frequencies, the two transfer functions disagree. Regions where a strong disagreement is observed are highlighted in gray. We thus explain the high frequency increase of the transfer functions in Figure 5 by measurement error of the ARGOS and GPS positioning systems of the buoys. Moreover, on Figure 4a, which considers a data set showing a large peak at the inertial frequency, we observe an apparent dissymmetry on the discrepancy between negative and positive part of the spectrum: this is explained by the fact that addition of noise can be neglected at frequencies where its amplitude is much less than the amplitude of the signal itself. For the same reason, on Figure 4b, where almost no peak is observed at the inertial frequency, such dissymmetry is not observed anymore and, because velocities are in average smaller for this data set, the mismatch between the two transfer functions starts earlier (at about 1.5 cycles.d$^{-1}$) and thus affects the value of the peak at the inertial frequency.

[19] As a consequence, it is important to note that, for transfer functions where a clear peak is observed at the inertial frequency, i.e., for most data sets, values of $|\hat{G}_b|$ are not affected in between $-2.2$ and $+1.5$ cycles.d$^{-1}$ while, for transfer functions exhibiting no peak at the inertial frequency (mostly data set numbers 1, 3 and 5), the values of $|\hat{G}_b|$ at the inertial frequency may have been artificially increased by noise on the buoys positions, leading to an associated

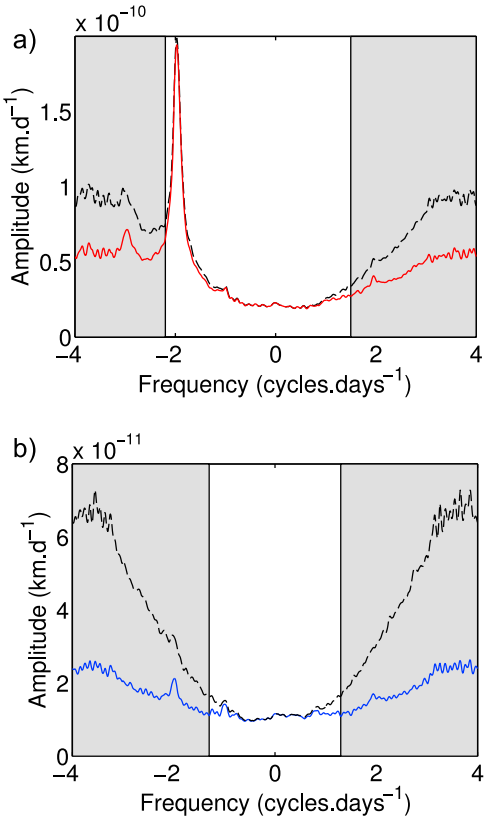


**Figure 4.** Illustration of the effect of the buoy position uncertainty on the transfer function using data sets (a) number 8 and (b) number 1. The red and blue bold curves are the transfer functions computed from the raw buoy positions. The black dashed curves are associated transfer functions computed using the respective data set, but after adding noise to the buoy positions (300 m standard deviation). We outline in gray the frequencies affected by the uncertainty on the buoys' positions.

underestimation of $K$ in these cases (see third paragraph of section 5.2).

## 5. Modeled Transfer Functions and Results

[20] In an unpublished paper (Gimbert et al., submitted manuscript, 2012), we argue that the sea ice inertial oscillation magnitude is a proxy of the degree of cohesiveness of the sea ice cover. In this study, in order to quantitatively investigate this consideration, the respective contributions of the ocean boundary layer and sea ice cover mechanical properties on the spatial, seasonal and pluriannual dependance of the inertial oscillations magnitude pointed out in (Gimbert et al., submitted manuscript, 2012) are evaluated through our analytical model presented in section 2. To do so, we split the model parameters into the following two categories:

[21] 1. The parameters we consider to be fixed or known: $C_{iw}$, $\gamma$, $h_i$ and $\alpha$. Appropriate values to consider for each data set are discussed in section 5.1. Values for $h_i$ and $\alpha$ are obtained from observations and thus vary from one data set to another, while, as the absence of direct observations induces large uncertainties on $C_{iw}$ and $\gamma$, their respective values are kept the same for all the eight data sets. A sensitivity analysis will be performed in section 6.1 on the values of $C_{iw}$ and $\gamma$.

[22] 2. The tuning parameters $h_w$ and $K$, on which we discuss the physics. As shown in third paragraph of section 5.2, these parameters $h_w$ and $K$ behave separately, allowing the determination of $h_w$ independently of the $K$ value considered.

[23] Under these considerations, we answer, in a first instance (section 5.2), the following questions:

[24] 1. Is the crude analytical model presented in section 2 able to reproduce the main features of sea ice motion in the frequency domain?

[25] 2. Is it needed, in addition to already accounted variations in the sea ice thickness $h_i$ and the sea ice concentration $\alpha$, to consider changes within the Ekman layer thickness $h_w$ and the internal sea ice friction coefficient $K$ in order to reproduce the transfer functions computed for the eight data sets? If yes, how $h_w$ and $K$ vary from one data set to another?

[26] Secondly, a sensitivity analysis (section 6.2) is performed in order to answer to the reciprocal question asked in the second point: can we explain the observations by varying only $C_{iw}$ and $\gamma$, instead of $K$?

### 5.1. Fixed Parameters

[27] The average values of sea ice thickness $h_i$ for each data set are listed in Table 1. They are obtained from *Rothrock et al.* [2008]. The sea ice concentration is computed at each buoy position from the sea ice concentration data set collected by the National Snow and Ice Data Center (http://nsidc.org/data/seaice/index.html), using the same procedure as the one described in section 4.2 of (Gimbert et al., submitted manuscript, 2012). Then, an average concentration value $\alpha$ is associated to each data set by averaging all the concentration values associated to each buoy position.

[28] In contrast to $\alpha$ and $h_i$, direct observations of $C_{iw}$ and $\gamma$ are missing. The drag $C_{iw}$ related to the linear friction is taken as $5.10^{-4}$ m.s$^{-1}$, following previous studies [*Weatherly et al.*, 1998; *Heil and Hibler*, 2002]. This value might be affected by changes in basal ice roughness, for instance if sea ice is more or less fractured. Nonetheless, we will see in section 6 that $C_{iw}$ is unlikely to have varied substantially.

[29] Estimating a value of $\gamma$ suitable for the Arctic basin is more difficult. Indeed, such estimates are absent from the literature. The parameter $\gamma$ is related to the decay timescale $\mathcal{T} = h_w/\gamma$ that corresponds to the e-folding time of ocean-only free inertial oscillations (see solution of equation (3) if $\alpha$ = 0 and $\tilde{U}_i$ = 0). Equatorward of the polar circle, $\mathcal{T}$ is usually found between 2 and 20 days [*D'Asaro*, 1985], which, for a typical $h_w$ = 50 m, corresponds to $\gamma$ between $3.10^{-4}$ and $3.10^{-5}$ m.s$^{-1}$. However, $\mathcal{T}$ is usually used as a tuning parameter rather than being physically based. The decay timescale $\mathcal{T}$ is related to 2 distinct processes: the turbulence production by vertical current shear, and the radiation of internal waves toward the thermocline (through the so called inertial pumping [*Price*, 1983]). Wave propagation plays the dominant role when rapid decay occurs, the case

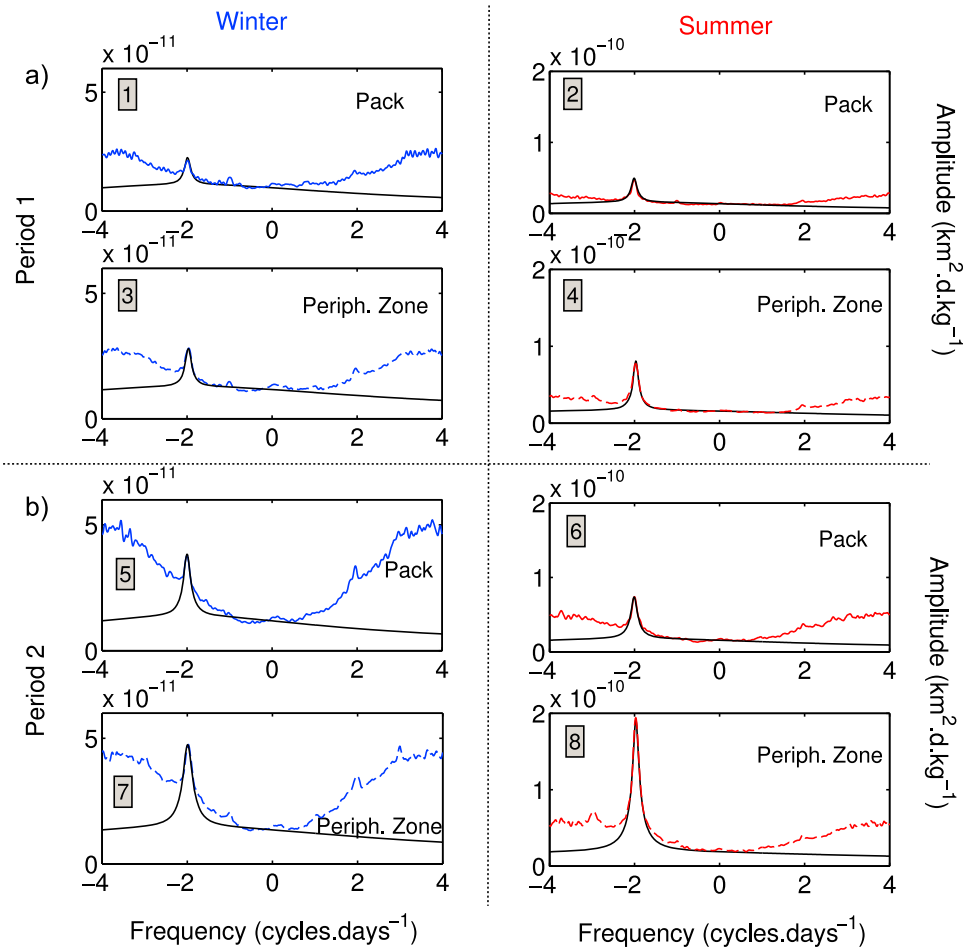


**Figure 5.** Modulus of the transfer functions of the buoy trajectories for the eight data sets. The bold and dashed lines indicate the transfer functions computed using buoy trajectories selected within the central pack zone and within the peripheral zone, respectively. The transfer functions averaged over (a) period 1 and (b) period 2 are computed (left) from the winter data sets (blue curves) and (right) from the summer data sets (red curves). The modeled transfer functions computed using equation (4) and parameters of Table 1 are plotted in black.

for which *Park et al.* [2009] have managed to link $\mathcal{T}$ to the ocean characteristics

$$\mathcal{T} \sim \left( \frac{\omega_0}{\beta^2 h_w^2 N^2} \right)^{1/3}. \quad (6)$$

[30] The right hand side (RHS) of (6) can be estimated from the ocean reanalysis GLORYS1 (Global Eddy Permitting Ocean Reanalysis and Simulation [*Ferry et al.*, 2010]), which has been used in the Arctic basin by *Lique et al.* [2010]. To estimate $h_w$ in equation (6), we use a density criteria rather than the temperature criteria used by *Park et al.* [2009], because the mixed-layer depth is strongly controlled by salinity in the Arctic [*Rudels et al.*, 1996]. Hence, the depth $h_w$ is taken as the depth over which the potential density $\sigma_0$ does not vary by more than 0.01 kg.m$^{-3}$ as compared to the surface. Typical winter and summer temperature and salinity profiles from GLORYS1 are shown in Figure 6b with the related mixed layer depths. Climatological values of $h_w$ are shown in Figure 6a, together with the RHS of (6). Figure 6a shows that if the theory of *Park et al.* [2009] is extended northward of the Arctic circle, the decay timescale $\mathcal{T}$ is expected to be much longer than the maximum of 20 days that they found near 60°N. Hence, $\mathcal{T}$ is probably controlled by the vertical current shear and observations show very small vertical mixing rates in the Arctic as compared to lower latitudes [*Gregg*, 1989; *Rainville and Winsor*, 2008; *Fer*, 2009]. Hence, we have to choose a value of $\gamma$ that gives decay timescales $\mathcal{T}$ longer than 20 days. With a maximum $h_w$ of 50 m (Figure 6a), it can be estimated that $\gamma > 3.10^{-5}$ m.s$^{-1}$ in the Arctic basin. In the following, we first use an order of magnitude for $\gamma$ of $10^{-5}$ m.s$^{-1}$. The sensitivity of our model's results to a varying $\gamma$ will be discussed in section 6.1.

[31] The mixed layer term of equation (3) with no wind forcing ($\tilde{\tau} = 0$) shows that the decay timescale of ocean currents (in the absence of forcing) depends on $\gamma$ and $C_{iw}$. The values that have been taken for these parameters ensure that the decay of ocean currents is controlled by $C_{iw}$, since $C_{iw} \gg \gamma$. This is in good agreement with the results found by

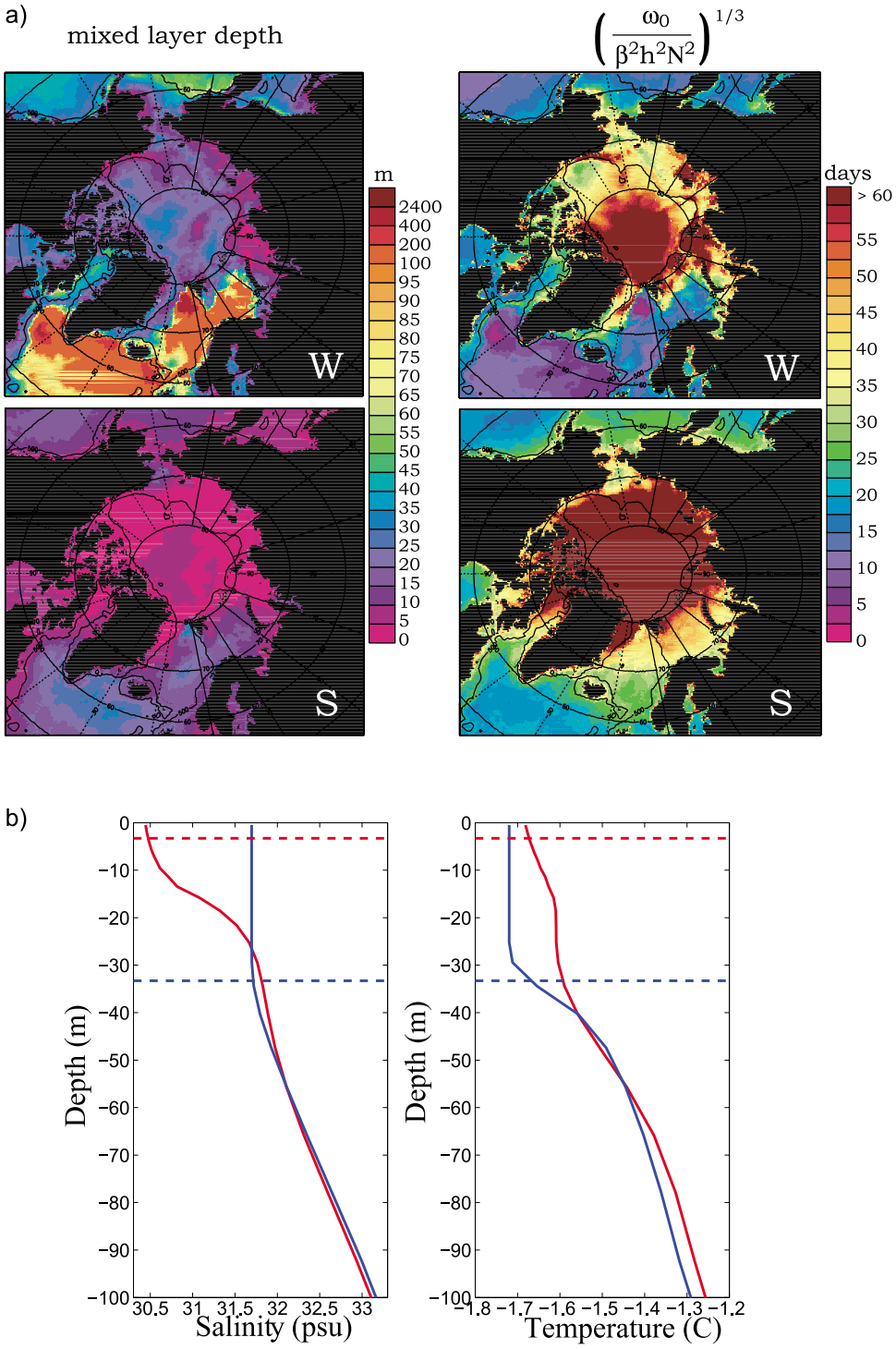


**Figure 6.** Oceanic parameter evaluated using GLORYS1. (a) (left) Mixed layer depth, in meters, defined using a density criteria and (right) right hand side of equation (6), in days. The winter (W) season and the summer (S) season are shown. Summer stands for July–August–September, and winter for the other months of the climatology. The climatology is computed using monthly means of the 2002–2008 ocean-sea ice reanalysis GLORYS1 [*Ferry et al.*, 2010] and a density criteria of 0.01 kg.m$^{-3}$. The buoyancy frequency $N^2$ in equation (6) is computed using the maximum stratification in the whole water column. (b) Salinity and temperature profiles at North Pole, from monthly climatological fields from GLORYS1 in August (summer, in red) and February (winter, in blue). The mixed layer depth calculated using the density criteria of 0.01 kg.m$^{-3}$ is indicated by the dashed lines.

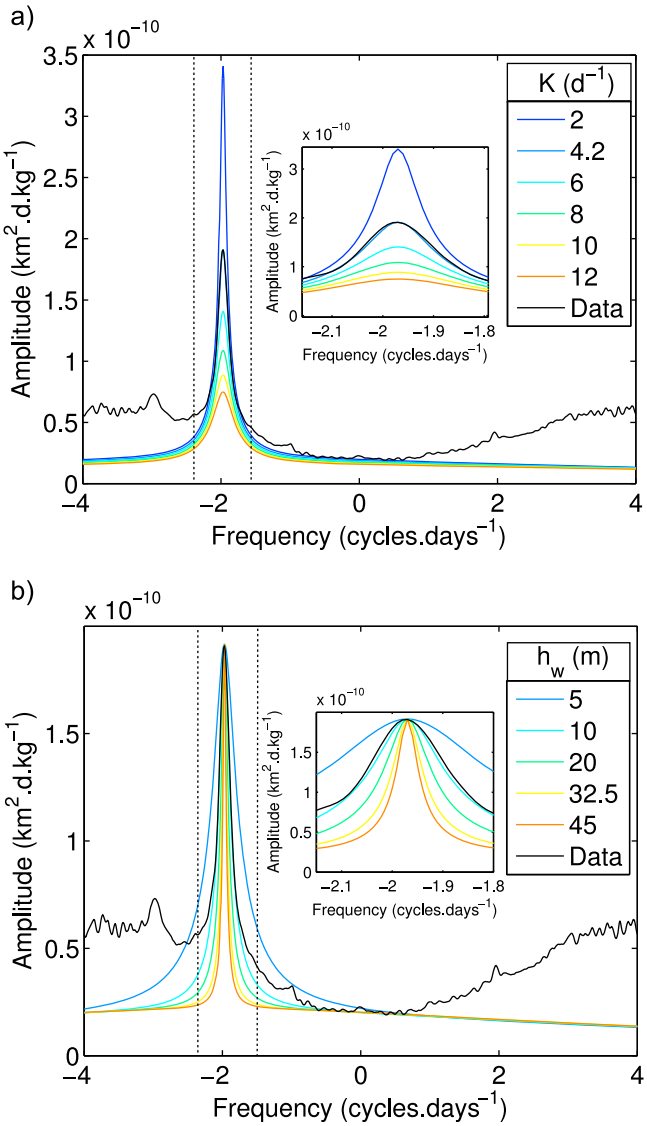


**Figure 7.** Influence of the tuning parameters on the shape of the transfer function for data set number 8. (a) Influence of the sea ice cover internal friction $K$ fixing $h_w$ =12.5 m and (b) influence of the Ekman layer thickness $h_w$ fixing $K$ = 1.2 days$^{-1}$. For both plots, the data transfer functions are plotted in black. A zoom around the inertial frequency $-f_0$ is done for each plot. The known parameters used are those considered for data set number 8 in Table 1.

*Pinkel* [2005] using a linear model of near-inertial wave propagation and observations in the Arctic.

### 5.2. Results and Interpretation

[32] Figure 5 shows the modulus of the transfer functions computed from the data, as well as the one modeled by using the tuning parameter values $K$ and $h_w$ that give the best fit (in the mean least square sense) for frequencies ranging from $-2.2$ cycles.d$^{-1}$ to 1 cycles.d$^{-1}$. The parameters used to reproduce the transfer functions for each of the eight data sets are detailed in Table 1. We can see the following:

[33] 1. In general, for all eight data sets, the model of equation (5) accounts well for the observed transfer function within the frequency range of $-2.2$ cycles.d$^{-1}$ to 1 cycles.d$^{-1}$. This is not the case outside this window, due to the result of noise on the buoys' positions (see section 4.3).

[34] 2. This simple linear model works better for summer data sets, when sea ice is closer to a free drift configuration, i.e., when sea ice remains closer to a fluid-like linear behavior. However, the agreement is still good for the winter data sets, at least for data set numbers 3, 5 and 7. This means that a simple linear formulation of the internal sea ice friction is able to reproduce the main features of the sea ice cover average mechanical response in the frequency domain. For the winter ice pack of period 1 (data set number 1), the agreement is less convincing. This sets the limit of the present linear model to describe the elasto-brittle rheology of sea ice [*Weiss et al.*, 2007; *Girard et al.*, 2011], even after averaging at large spatial and timescales.

[35] 3. Setting typical values for $C_{iw}$, $\gamma$, $h_i$ and $\alpha$, both $K$ and $h_w$ need to vary from one data set to the other to best fit. To highlight this point, Figure 7 plots the data transfer function of data set number 8 along with the modeled one by fixing $h_w$ and varying the values of $K$ (Figure 7a) and by fixing $K$ and varying the values of $h_w$ (Figure 7b). From these two plots, it is obvious that the two parameters $K$ and $h_w$ work separately: $K$ controls the amplitude of the transfer function peak at the frequency $f = -f_0$ and, to a lesser extent, the level of the plateau at low frequency, while $h_w$ only affects the width of the peak at $f = -f_0$, without affecting its amplitude nor the plateau at low frequencies. Thus, for a value of $K$ that leads to a good estimate of the data transfer function at $f = -f_0$ and $f = 0$, the tuning of $h_w$ further allows to get a good agreement in the surroundings of $-f_0$.

[36] Because noise on the buoy positions may have increased the amplitude of the peak at the inertial frequency for data set numbers 1, 3 and 5, it is important to notice that the associated values of $K$ are likely to be underestimated in these cases.

[37] 4. Changes within sea ice dynamic reported by *Rampal et al.* [2009] with respect to time and space are associated not only to changes in the sea ice thickness $h_i$ and the sea ice concentration $\alpha$, which are parameters already taken into account in the momentum balance of our model, but also to changes in the sea ice internal friction $K$ and the ocean Ekman layer thickness $h_w$.

[38] The friction coefficient $K$ is strongly decreased from winter to summer, in the central ice pack as well as in the peripheral zone. This means that the sea ice mechanical behavior varies drastically with the season, independently of the region considered. This is in agreement with the annual cycle described by the $M$ values in (Gimbert et al., submitted manuscript, 2012).

[39] Wether it is for period 1 or period 2 and in summer or in winter, $K$ seems to be independent of the region considered. This suggests that the large inertial oscillation amplitudes observed in summer in the peripheral zone (see (Gimbert et al., submitted manuscript, 2012)) essentially result from a direct effect of ice thinning and decreasing concentration on the momentum balance, and shows that there is no contrast of mechanical behavior between multiyear and first-year sea ice.

[40] Finally, whatever the season or the region considered, $K$ decreased by a factor of 1.5 from period 1 to period 2. As an example, the mechanical behavior of winter sea ice in

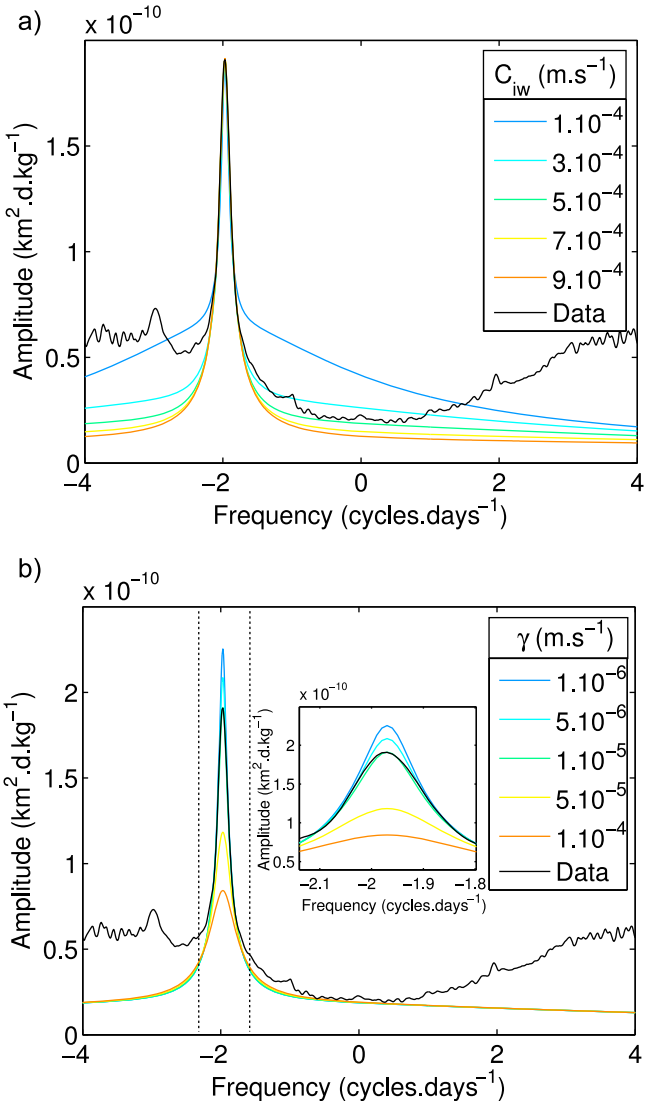


**Figure 8.** (a) Influence of the drag coefficient $C_{iw}$ and (b) influence of the turbulent viscosity $\gamma$ on the shape of the transfer function for data set number 8. For both plots, the data transfer functions are plotted in black. A zoom around the inertial frequency $-f_0$ is done in Figure 8b. The other known and tuning parameters used are those considered for data set number 8 in Table 1.

recent years is comparable to that of summer sea ice in previous years.

[41] For all that, considering the eight data sets, we obtain an anticorrelation of $\xi = -0.75$ between the $M$ and $K$ values. The probability to find a lower correlation coefficient is estimated to 0.25% by randomly reshuffling the values, proving that this correlation is significant. This means that the previously defined $M$ parameter (Gimbert et al., submitted manuscript, 2012) is a simple and reasonably accurate proxy of the level of internal friction.

[42] We can thus conclude that the sea ice decline already pointed out by several authors [*Lindsay and Zhang*, 2005; *Comiso et al.*, 2008; *Kwok and Rothrock*, 2009; *Rampal et al.*, 2009] is not restricted to a decrease of sea ice concentration and sea ice thickness, but is accompanied by a mechanical weakening of the ice cover. As the direct effect of ice thinning and declining concentrations on the momentum balance is already taken into account in our model, this evolution is, we believe, an indirect effect of the ice state onto the ice internal friction through the degree of fragmentation of the ice cover.

[43] Concerning the oceanic boundary layer $h_w$, the order of magnitude as well as the seasonal and regional dependence obtained from our model within the second period are in good agreement with those obtained from GLORYS, shown on Figure 6, for the period 2002–2008: $h_w$ is of the order of 10 m within the peripheral zone in summer and of the order of several tens of meters (approximately 30–40 m) in winter within the central pack. Values of $h_w$ considerably decreased from period 1 to period 2, since it is almost divided by two whatever the season and the region. Thus, seasonal and decadal variations of the ocean mixed layer depth $h_w$ are observed. These variations are consistent with previous studies showing an enhanced stratification in the upper halocline when sea ice melts or when river runoffs are intense [*Rudels et al.*, 1996]. The stronger stratification may alter $h_w$ either because the criteria used to define $h_w$ ($\Delta\sigma_0 < 0.01$ kg.m$^{-3}$) is reached closer to the surface, or because the stronger stratification limits vertical mixing [*Stull*, 1988]. In these 2 cases, $h_w$ is decreased when ice melting and river runoff are increased, as found in GLORYS and in our parameter estimation. Such an explanation relates the evolution of $h_w$ to the evolution of the salinity barrier. A more complete picture of the evolution of $h_w$ would include evolution of the mechanical forcing of $h_w$, through the estimation of the production of turbulent kinetic energy $\gamma|\tilde{U}_w|$ within the ocean surface layer. Such an estimation can be done using our model and, since this study is out of the scope of this paper, these computations are presented in Appendix A.

## 6. Sensitivity Analysis

[44] We showed above that assuming typical values for $C_{iw}$ and $\gamma$, changes observed within the sea ice dynamical response to the inertial forcing are explained by tuning $K$ and $h_w$. However, since large uncertainties lie on $C_{iw}$ and $\gamma$, it is important to ask the following questions:

[45] 1. To what extent $K$ and $h_w$ vary when considering different values for $\gamma$ and $C_{iw}$? Is the hierarchy in the $K$ values obtained for the different data sets conserved in these cases?

[46] 2. Can the observations be explained by changing $\gamma$ and $C_{iw}$, while keeping $K$ constant over all data sets?

### 6.1. Sensitivity on $\gamma$ and $C_{iw}$

[47] Figure 8a shows the influence of $C_{iw}$ on the shape of the transfer function. When varying the values of $C_{iw}$ of 1 order of magnitude around the typical value of $5.10^{-4}$ m.s$^{-1}$, this shape is largely affected, at all frequencies. This implies that the value of $C_{iw}$ is robust and well constrained. This is confirmed when trying to fit all 8 data sets by allowing $K$, $h_w$ and $C_{iw}$ to vary: in that case, the values of $C_{iw}$ giving the best fits only vary from $3.5.10^{-4}$ m.s$^{-1}$ to $4.6.10^{-4}$ m.s$^{-1}$. Figure 8b shows the influence of $\gamma$ on the transfer function: in addition to $K$, $\gamma$ controls the amplitude of the peak at $f = -f_0$

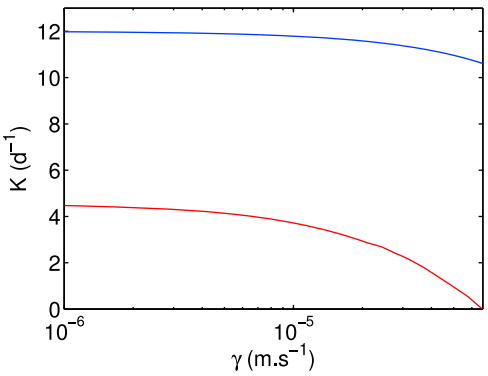


**Figure 9.** $K$ versus $\gamma$ for data set numbers 1 (blue line) and 8 (red line), for $\gamma$ ranging between $1.10^{-6}$ m.s$^{-1}$ and $6.7.10^{-5}$ m.s$^{-1}$ and taking $C_{iw} = 5.10^{-4}$ m.s$^{-1}$. The best fit of the data transfer functions for each $\gamma$ value is obtained by only tuning the internal sea ice cover friction $K$, with $h_w$ as in Table 1.

as well. We thus consider $C_{iw} = 5.10^{-4}$ m.s$^{-1}$ to be a robust value and limit, in this section, our sensitivity analysis to the study of the parameter $\gamma$, since it qualitatively plays the same role as $K$ on the transfer function.

[48] We start by defining a lower and upper bounds for $\gamma$. The lower bound is arbitrarily chosen to be equal to $1.10^{-6}$ m.s$^{-1}$, which is 1 order of magnitude lower than the value taken into account in section 5.2. The upper bound is set from the observations: indeed, the amplitude of the peak at the inertial frequency $-f_0$ for data set number 8 cannot be reproduced when considering a value of $\gamma$ greater than $6.7.10^{-5}$ m.s$^{-1}$. We thus consider $\gamma = 6.7.10^{-5}$ m.s$^{-1}$ as an upper bound. Such a value gives $K = 0$ d$^{-1}$ for data set number 8, which means that, in this case, sea ice exactly behaves in free drift within the peripheral zone during the second period. We thus assume that $\gamma$ can vary between $1.10^{-6}$ m.s$^{-1}$ and $6.7.10^{-5}$ m.s$^{-1}$.

[49] Figure 9 shows the variation of $K$ with respect to $\gamma$ for data sets number 1 and number 8. For data set number 1, we can see that the value of $K$ does not vary considerably with $\gamma$: the internal friction that takes place within the sea ice cover dominates compared to the damping that takes place within the oceanic Ekman layer. On the contrary, for data set number 8, the turbulent viscosity $\gamma$ strongly influences the value of $K$. $K$ ranges from about 4 days$^{-1}$ to 0 days$^{-1}$ as $\gamma$ increases from $1.10^{-6}$ m.s$^{-1}$ to $6.7.10^{-5}$ m.s$^{-1}$. It is also clear from Figure 9 that $K$ values would not significantly change when considering $\gamma$ values below$1.10^{-6}$ m.s$^{-1}$, whatever the data set considered. The $K$ values obtained for the eight data sets when considering $\gamma = 6.7.10^{-5}$ m.s$^{-1}$ are given in Table 2. The hierarchy between the different data sets, and therefore the associated interpretation, is conserved compared to that of Table 1 and section 5.2. We note however that with such large value of $\gamma$ the associated decay timescales $\mathcal{T} = h_w/\gamma$ vary between 2 to 8 days, i.e., are small compared to expected values in the Arctic (see section 5.1).

### 6.2. Can *K* be Constant?

[50] Choosing a fixed value for $K$, we now try to explain the eight data sets by allowing $C_{iw}$ and $\gamma$ to vary simultaneously.

[51] 1. Assuming $K = 1$ days$^{-1}$, $C_{iw}$ has to vary between $4.2.10^{-4}$ m.s$^{-1}$ (data set number 8) and $8.8.10^{-4}$ m.s$^{-1}$ (data set number 1), and $\gamma$ between $1.9.10^{-3}$ m.s$^{-1}$ (data set number 1) to $5.4.10^{-5}$ m.s$^{-1}$ (data set number 8). The values of $C_{iw}$ are reasonable, since they vary within a factor of two around the typical value $C_{iw} = 5.10^{-4}$ m.s$^{-1}$. However, considering the values of $h_w$ of Table 1, such variations for $\gamma$ lead to variations of the decay timescale $\mathcal{T} = h_w/\gamma$ between 0.3 day (data set number 1) and 2 days (data set number 8), which we cannot accept for two reasons: first, changes in the decay timescale of 1 order of magnitude at similar latitudes are difficult to explain and, secondly, these values are very small, i.e., 1–2 orders of magnitude lower than the lower bound value of 20 days discussed previously (section 5.1) from the observations of *Park et al.* [2009] near 60°N (see section 5.1; such values for $\mathcal{T}$ are even smaller than typical values found for tropical regions [*Park et al.*, 2009]).

[52] 2. By assuming $K = 10$ days$^{-1}$, negative values of $\gamma$ are required to explain data set number 8, which is non sense.

[53] Consequently, changes in the sea ice internal friction with the hierarchy discussed above are required to explain the observations from our ocean boundary layer-sea ice dynamical model.

## 7. Conclusion

[54] In an unpublished paper (Gimbert et al., unpublished paper, 2011), we analyzed the magnitude of inertial oscillations over the Arctic sea ice cover from the IABP buoy trajectories data set covering three decades (1979–2008). A seasonal and regional dependence of this magnitude of inertial oscillation was observed: larger oscillations are associated to thinner, less cohesive sea ice, such as in summer and/or in the peripheral zone of the Arctic basin. We therefore proposed that the sea ice response to the constant inertial forcing could be used to investigate its average mechanical behavior; a weak, poorly cohesive cover being characterized by strong inertial motion. We also observed a remarkable strengthening of inertial motion in recent years (since 2002), especially in the peripheral zone of the Arctic basin where sea ice decline has been particularly marked, which we therefore interpreted as a mechanical weakening of the sea ice cover.

[55] In the present paper, we proposed a simple ocean boundary layer-sea ice coupled dynamical model that we apply to the modeling of Arctic sea ice motion in the frequency domain, and particularly in the inertial range. In this model, the sea ice mechanical response is simplified through the introduction of a linear friction term $K$. This model allows particularly to discriminate the direct effect of ice thinning and decreasing concentration onto the momentum balance of the ice cover, and the effect of the ice internal friction that we aim to analyze. The main conclusions of this work are as follows:

[56] 1. The proposed coupled dynamical model well describes sea ice motion in the frequency domain from inertial motion to advection motion, when averaged over large time (season) and spatial (1000 km) scales from IABP buoy trajectories. The accuracy is less good for the central pack in winter, for which the nonlinear brittle rheology of

**Table 2.** $K$ Values Computed From the Model by Considering $C_{iw} = 5.10^{-4}$ m.s$^{-1}$, as in Table 1, and $\gamma = 6.7.10^{-5}$ m.s$^{-1}$[a]

| | | | | Fixed Parameters | | Tuning Parameters | | | |
|---|---|---|---|---|---|---|---|---|---|
| | Zone | Season | Data Set | $h_i$ (m) | $\alpha$ | $K$ (days$^{-1}$) | $h_w$ (m) | $\mathcal{T}$ (days) | $M$ |
| Period 1 | Pack zone | Winter | 1 | 4 | 0.98 | 10.5 | 45 | 8 | 0.1514 |
| | Pack zone | Summer | 2 | 3 | 0.9 | 6 | 35 | 6 | 0.172 |
| | Peripheral zone | Winter | 3 | 3 | 0.96 | 10.5 | 45 | 8 | 0.156 |
| | Peripheral zone | Summer | 4 | 2 | 0.82 | 5 | 25 | 6 | 0.244 |
| Period 2 | Pack zone | Winter | 5 | 3.5 | 0.96 | 6 | 30 | 5 | 0.182 |
| | Pack zone | Summer | 6 | 2.5 | 0.84 | 3.5 | 25 | 4 | 0.220 |
| | Peripheral zone | Winter | 7 | 2.5 | 0.95 | 7 | 20 | 3 | 0.202 |
| | Peripheral zone | Summer | 8 | 1.5 | 0.62 | 0 | 10 | 2 | 0.371 |

[a]This value for $\gamma$ is the upper bound when considering $C_{iw} = 5.10^{-4}$ m.s$^{-1}$. The fixed model parameters considered as well as the Ekman boundary layer thickness $h_w$ obtained from the model are the same as those summed up in Table 1. The modeled transfer functions are adjusted compared to the data by tuning $K$ and $h_w$. Such a large value for $\gamma$ lead to decay timescales lower than 10 days for all data sets and corresponds to $K = 0$ days$^{-1}$ for data set number 8.

sea ice is not very well described by a linear friction term, even after averaging.

[57] 2. This model allows to explain the seasonal and regional dependence of Arctic sea ice inertial motion through an associated dependence of the internal friction $K$. $K$ is maximal for the thick multiyear ice pack in winter, and minimal in summer over a peripheral zone covered mainly nowadays by first-year ice.

[58] 3. A significant decrease of $K$, i.e., a genuine mechanical weakening of the sea ice cover, is observed for the period 2002–2008 compared to 1979–2001. Most notably, the mechanical behavior of winter sea ice in recent years is comparable to that of summer sea ice in previous years.

[59] 4. The observed IABP average spectra of ice motion cannot be correctly modeled by varying parameters such as the ocean-ice friction coefficient ($C_{iw}$) or the damping term within the ocean boundary layer ($\gamma$), while keeping $K$ constant. In other words, an annual and interannual dependence of the ice internal friction is the only way to explain the observations.

[60] 5. This coupled dynamical model can also be used to estimate the thickness of the oceanic boundary layer $h_w$, independently of the determination of $K$. We obtained thicknesses of the order of 10 m within the peripheral zone in summer, and of several tens of meters in winter within the central pack. Values of $h_w$ also considerably decreased from the period 1979–2001 to recent years (2002–2008), by a factor of about 2. These variations are consistent with an enhanced stratification in the upper halocline when sea ice melts or when river runoffs are intense.

[61] In conclusion, the evolution of Arctic sea ice in recent years in terms of extent, concentration or thickness, is accompanied by a mechanical weakening of the cover at the basin scale. These two aspects are coupled, as a weaker ice deforms and drifts more easily, thus enhancing sea ice export out of the basin as well as lead opening that strengthen the positive albedo feedback in summer. This, in turn, has a negative impact on sea ice balance, ice thickness, and concentration [*Rampal et al.*, 2011], so weakens the ice cover. This mechanical feedback most likely reinforces the sea ice decline.

## Appendix A: Estimating the Production of Turbulent Kinetic Energy Within the Ocean

[62] A more complete picture of the evolution of $h_w$ (described in section 5.2) must include evolution of the mechanical forcing of $h_w$. Though little is known about the Arctic, it has been shown that the erosion of a salt barrier at lower latitudes require strong mixing events rather than a slow mixing resulting from average winds [e.g., *McPhaden et al.*, 1992; *Zhang and McPhaden*, 2000]. Thus, the storm-induced inertial currents described by our model might be suitable to represent a part of the evolution of the mechanical forcing of $h_w$ (even though $h_w$ is constant in our model). Then, the term $\rho_w\gamma|\tilde{U}_w|^2$ (in W.m$^{-2}$) is likely to represent, by meter square, the rate of production of turbulent kinetic energy in our model, i.e., the mechanical forcing of $h_w$ if the latter were to vary. In this section, the variation of production of turbulent kinetic energy in the ocean is estimated by determining $|U_w|$ using the coupled model described in this paper.

[63] Similar calculations as in section 3 allow to express $|U_w|$ as

$$\hat{U}_w(\omega) = \frac{\tau}{\rho h_w} \frac{\frac{C_{iw}}{h_i} + (1-\alpha)K + i(1-\alpha)(\omega+\omega_0)}{\left[\left(-(\omega+\omega_0)^2 + \frac{1}{h_w}(\alpha C_{iw}+\gamma)\left(K+\frac{C_{iw}}{h_i}\right) - \frac{\alpha C_{iw}^2}{h_i h_w}\right) + i(\omega+\omega_0)\left(\frac{C_{iw}}{h_i}+\frac{\alpha C_{iw}}{h_w}+\frac{\gamma}{h_w}+K\right)\right]}, \tag{A1}$$

where $\omega = 2\pi f$ and $\rho_i = \rho_w = \rho$ is assumed. The respective values of $|U_w|$ for the eight data sets are plotted on Figure A1, using the wind stress Fourier spectrum computed in section 4.2 and the parameters summed up in Table 1. As stated in section 4.2, the atmospheric forcing does not vary much among the eight data sets. By contrast, $|\tilde{U}_w|$ shows the following substantial variations: (1) in the peripheral zone and in summer, the magnitude of $|\tilde{U}_w|$ increased by a factor of 2 from period 1 to period 2; the value of $|\tilde{U}_w|$ at the inertial frequency goes from 1.5 m.s$^{-1}$ to 3 m.s$^{-1}$ and (2) on the contrary, for the other data sets, i.e., in the central pack or in the peripheral zone in winter, the magnitude of $|\tilde{U}_w|$ is very small compared to the values

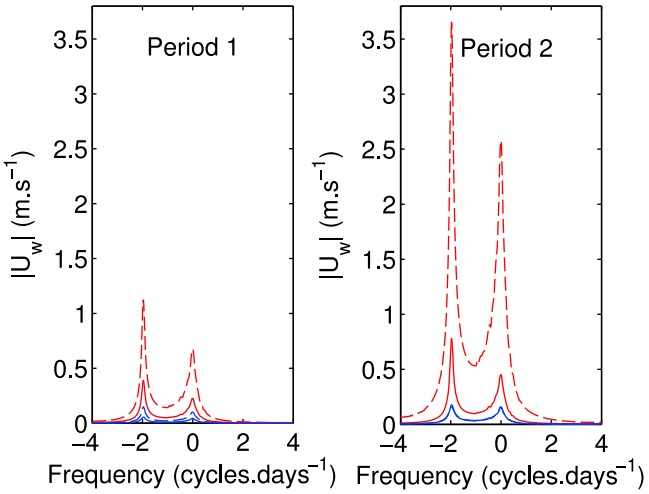


**Figure A1.** Amplitude of the Fourier transform of $U_w$ computed for the eight data sets from the model by using the parameter values summed up in Table 1 and the wind stress Fourier transforms presented in section 4.2. The bold and dashed lines indicate the Fourier transforms computed using buoy trajectories selected within the central pack zone and within the peripheral zone, respectively. The blue and red lines indicate the Fourier transforms computed using buoy trajectories selected in winter and in summer, respectively.

computed in the peripheral zone and in summer and does not vary that much between the different data sets.

[64] This shows that the production of inertial currents at the ocean surface is mainly controlled by the concentration of open water. The production of stronger inertial currents are modeled for larger values of open water concentration. This effect would have increased the mixed layer depth from period 1 to period 2 if the surface freshwater flux had not changed. However, both our estimates and GLORYS show a decrease of the mixed layer depth from period 1 to period 2. This means that the effect of increased inertial currents is smaller than the inhibition effect on mixing caused by an increase in sea-ice melt and river runoff. Nonetheless, the increase of $|\tilde{U}_w|$ from period 1 to period 2 means that the energy radiated toward the deep ocean through inertial waves is likely to have increased. As the interaction between these waves and the bottom topography is important for the properties of water masses in the Arctic (see Introduction), the increase of $|\tilde{U}_w|$ could be of climatic importance. However, more realistic studies would need to be carried out if this work were to be made more accurate.

[65] **Acknowledgments.** The ERA-Interim wind data set, provided in the frame of the Drakkar project, and the ocean reanalysis GLORYS have been kindly furnished by the team Mercator Ocean (http://www.mercator-ocean.fr/). We thank the two anonymous reviewers and the associate editor for their constructive comments.

## References

Alford, M. H. (2003), Improved global maps and 54-year history of wind-work on ocean inertial motions, *Geophys. Res. Lett.*, *30*(8), 1424, doi:10.1029/2002GL016614.

Comiso, J. C., C. L. Parkinson, R. Gersten, and L. Stock (2008), Accelerated decline in the Arctic sea ice cover, *Geophys. Res. Lett.*, *35*, L01703, doi:10.1029/2007GL031972.

D'Asaro, E. A. (1985), The energy flux from the wind to near-inertial motions in the surface mixed layer, *J. Phys. Oceanogr.*, *15*(8), 1043–1059.

D'Asaro, E. A., and J. H. Morison (1992), Internal waves and mixing in the Arctic Ocean, *Deep Sea Res. Part A*, *39*(2), S459–S484.

D'Asaro, E. A., C. C. Eriksen, M. D. Levine, P. Niiler, C. A. Paulson, and P. Van Meurs (1995), Upper-ocean inertial currents forced by a strong storm. Part I: Data and comparisons with linear theory, *J. Phys. Oceanogr.*, *25*(11), 2909–2936.

Elipot, S., and S. T. Gille (2009), Estimates of wind energy input to the Ekman layer in the Southern Ocean from surface drifter data, *J. Geophys. Res.*, *114*, C06003, doi:10.1029/2008JC005170.

Fer, I. (2009), Weak vertical diffusion allows maintenance of cold halocline in the central Arctic, *Atmos. Oceanic Sci. Lett.*, *2*(3), 148–152.

Ferry, N., L. Parent, G. Garric, B. Barnier, N. C. Jourdain, and the Mercator Ocean team (2010), Mercator Global Eddy Permitting Ocean Reanalysis GLORYS1V1: Description and results, *Mercator Q. Newsl.*, *36*, 15–27.

Garrett, C. (2001), What is the "near-inertial" band and why is it different from the rest of the internal wave spectrum?, *J. Phys. Oceanogr.*, *31*(4), 962–971.

Gent, P., K. O'Neill, and M. Cane (1983), A model of the semiannual oscillation in the equatorial Indian Ocean, *J. Phys. Oceanogr.*, *13*(12), 2148–2160.

Girard, L., S. Bouillon, J. Weiss, D. Amitrano, T. Fichefet, and V. Legat (2011), A new modelling framework for sea-ice mechanics based on elasto-brittle rheology, *Ann. Glaciol.*, *52*(57), 123–132.

Greatbatch, R. J. (1983), On the response of the ocean to a moving storm: The nonlinear dynamics, *J. Phys. Oceanogr.*, *13*, 357–367.

Greatbatch, R. J. (1984), On the response of the ocean to a moving storm: Parameters and scales, *J. Phys. Oceanogr.*, *14*(1), 59–78.

Gregg, M. C. (1989), Scaling turbulent dissipation in the thermocline, *J. Geophys. Res.*, *94*(C7), 9686–9698.

Heil, P., and W. D. Hibler III (2002), Modeling the high-frequency component of Arctic sea ice drift and deformation, *J. Phys. Oceanogr.*, *32*(11), 3039–3057.

Hibler, W. D. (1979), A dynamic thermodynamic sea-ice model, *J. Phys. Oceanogr.*, *9*, 815–846.

Kwok, R., and D. A. Rothrock (2009), Decline in Arctic sea ice thickness from submarine and icesat records: 1958–2008, *Geophys. Res. Lett.*, *36*, L15501, doi:10.1029/2009GL039035.

Lenn, Y., T. Rippeth, C. Old, S. Bacon, I. Polyakov, V. Ivanov, and J. Holemann (2011), Intermittent intense turbulent mixing under ice in the Laptev Sea continental shelf, *J. Phys. Oceanogr.*, *41*(3), 531–547.

Lepparanta, M. (2004), *The Drift of Sea Ice*, Springer, Berlin.

Lindsay, R. W., and J. Zhang (2005), The thinning of Arctic sea ice, 1988–2003: Have we passed a tipping point?, *J. Clim.*, *18*(22), 4879–4894, doi:10.1175/JCLI3587.1.

Lique, C., A. M. Treguier, G. Garric, B. Barnier, F. Girard-Ardhuin, N. Ferry, and C. E. Testut (2010), Evolution of the Arctic Ocean salinity, 2007–2008: Contrast between the Canadian and the Eurasian basins, *J. Clim.*, *24*(6), 1705–1717, doi:10.1175/2010JCLI3762.1.

McPhaden, M., F. Bahr, Y. Du Penhoat, E. Firing, S. Hayes, P. Niiler, P. Richardson, and J. Toole (1992), The response of the western equatorial Pacific Ocean to westerly wind bursts during November 1989 to January 1990, *J. Geophys. Res*, *97*, 14,289–14,303.

McPhee, M., and L. Kantha (1989), Generation of internal waves by sea ice, *J. Geophys. Res.*, *94*(C3), 3287–3302.

Park, J. J., K. Kim, and R. W. Schmitt (2009), Global distribution of the decay timescale of mixed layer inertial motions observed by satellite-tracked drifters, *J. Geophys. Res.*, *114*, C11010, doi:10.1029/2008JC005216.

Pinkel, R. (2005), Near-inertial wave propagation in the western Arctic, *J. Phys. Oceanogr.*, *35*(5), 645–665.

Plueddemann, A. J., and J. T. Farrar (2006), Observations and models of the energy flux from the wind to mixed-layer inertial currents, *Deep Sea Res. Part II*, *53*(1–2), 5–30.

Pollard, R. T., and J. R. C. Millard (1970), Comparison between observed and simulated wind-generated inertial oscillations, *Deep Sea Res. Oceanogr. Abstr.*, *17*, 813–816.

Price, J. F. (1983), Internal wave wake of a moving storm. Part I: Scales, energy budget and observations, *J. Phys. Oceanogr.*, *13*, 949–965.

Rainville, L., and P. Winsor (2008), Mixing across the Arctic Ocean: Microstructure observations during the Beringia 2005 expedition, *Geophys. Res. Lett.*, *35*, L08606, doi:10.1029/2008GL033532.

Rampal, P., J. Weiss, and D. Marsan (2009), Positive trend in the mean speed and deformation rate of Arctic sea ice, 1979–2007, *J. Geophys. Res.*, *114*, C05013, doi:10.1029/2008JC005066.

Rampal, P., J. Weiss, C. Dubois, and J.-M. Campin (2011), IPCC climate models do not capture Arctic sea ice drift acceleration: Consequences in terms of projected sea ice thinning and decline, *J. Geophys. Res.*, *116*, C00D07, doi:10.1029/2011JC007110.

Richter-Menge, J. A., and B. C. Elder (1998), Characteristics of pack ice stress in the Alaskan Beaufort Sea, *J. Geophys. Res.*, *103*(C10), 21,817–21,829, doi:199810.1029/98JC01261.

Richter-Menge, J. A., S. L. McNutt, J. E. Overland, and R. Kwok (2002), Relating arctic pack ice stress and deformation under winter conditions, *J. Geophys. Res.*, *107*(C10), 8040, doi:10.1029/2000JC000477.

Rothrock, D. A., D. B. Percival, and M. Wensnahan (2008), The decline in Arctic sea-ice thickness: Separating the spatial, annual, and interannual variability in a quarter century of submarine data, *J. Geophys. Res.*, *113*, C05003, doi:10.1029/2007JC004252.

Rudels, B., L. G. Anderson, and E. P. Jones (1996), Formation and evolution of the surface mixed layer and halocline of the Arctic Ocean, *J. Geophys. Res.*, *101*(C4), 8807–8821.

Stroeve, J., M. Serreze, S. Drobot, S. Gearheard, M. Holland, J. Maslanik, W. Meier, and T. Scambos (2008), Arctic sea ice extent plummets in 2007, *Eos Trans. AGU*, *89*(2), 13, doi:10.1029/2008EO020001.

Stull, R. B. (1988), *An Introduction to Boundary Layer Meteorology*, Kluwer Acad., Dordrecht, Netherlands.

Watanabe, M., and T. Hibiya (2002), Global estimates of the wind-induced energy flux to inertial motions in the surface mixed layer, *Geophys. Res. Lett.*, *29*(8), 1239, doi:10.1029/2001GL014422.

Weatherly, J. W., B. P. Briegleb, W. G. Large, and J. A. Maslanik (1998), Sea ice and polar climate in the NCAR CSM, *J. Clim.*, *11*(6), 1472–1486.

Weiss, J., E. M. Schulson, and H. L. Stern (2007), Sea ice rheology from in-situ, satellite and laboratory observations: Fracture and friction, *Eart Planet. Sci. Lett.*, *255*(1–2), 1–8, doi:10.1016/j.epsl.2006.11.033.

Young, W. R., and M. Ben Jelloul (1997), Propagation of near-inertial oscillations through a geostrophic flow, *J. Mar. Res.*, *55*, 735–766.

Zhang, C., and M. J. McPhaden (2000), Intraseasonal surface cooling in the equatorial western Pacific, *J. Clim.*, *13*(13), 2261–2276.